200712045A

別添1

厚生労働科学研究費補助金

医療機器開発推進研究事業

がん微小環境制御を併用したナノドラッグによる難治性固形がん治療の実現
(H19-ナノ-若手-001)

平成１９年度　総括研究報告書

主任研究者　狩野　光伸

平成２０（２００８）年　４月

別添2

目　　次

Ⅰ．総括研究報告

がん微小環境制御を併用したナノドラッグによる難治性固形がん治療の実現

---------- 1

狩野光伸

II. 分担研究報告

白金錯体制ガン剤DACHPtを内包した高分子ミセルの構築

---------- 4

西山伸宏

III. 研究成果の刊行に関する一覧表 ---------- 6

Ⅳ．研究成果の刊行物・別刷 ---------- 7

別添３

厚生労働科学研究費補助金（医療機器開発推進研究事業）

総括研究報告書

がん微小環境制御を併用したナノドラッグによる難治性固形がん治療の実現

主任研究者　狩野　光伸

（東京大学大学院医学系研究科分子病理学講座　ナノバイオ・インテグレーション研究拠点特任助教）

研究要旨：腫瘍標的ナノDDS開発において固形癌での蓄積向上は大きな課題であるが、現状は、一部の腫瘍でしか十分な効果は証明されていない。本研究ではナノDDSの効果を規定するEPR効果の要素、すなわち血管など腫瘍間質の構成要素を特異的に制御することで、一般臓器への薬剤蓄積の増悪なく、特に難治性固形癌でのナノDDS貯留増強を実現することを目的とする。

分担研究者　西山　伸宏

（東京大学大学院医学系研究科　疾患生命工学センター　臨床医工学部門　講師）

A．研究目的

ナノ粒子の腫瘍内蓄積については、現在多用されているC26マウス大腸癌細胞皮下移植モデルなどでの腫瘍血管における知見すなわち、全ての腫瘍血管が数百nmの物質に対して漏出性であるという前提で開発されてきた。米国のJainらによる学説(Jain RK et al, Science, 307:58-62 (2005)他)によれば、物質の腫瘍内移行を増加させる方法として、腫瘍血管を血管内皮増殖因子(VEGF)阻害剤によって正常化するのが妥当であるとされる。

この学説に対して、我々の研究（Kano MR et al. PNAS 104:3460-3465 (2007)）では、難治がんである膵がんおよび胃がんの腫瘍血管では実は漏出性は高くなく、逆に漏出性を増加させた方が、ナノ粒子の腫瘍蓄積が増強される可能性を示唆した。これら腫瘍モデルではVEGF阻害剤併用は効果を示さなかった。

そこで本研究は、これら腫瘍血管を含む腫瘍微小環境すなわちEnhanced Permeability and Retention Effect (EPR効果)の要素に着目し、その制御の併用により、副作用の増悪なく難治性固形癌でのナノDDSの薬効を増強することを目指す。

B．研究方法

本年度は以下について着手した：1．難治性でない固形癌でも増強効果があるか。2．膵癌・胃癌以外の難治性固形癌での併用効果はあるか。3．がん新生リンパ管制御はナノDDSの分布増強効果があるか。4．より薬剤として有効かつトレーサーにも用いることのできるナノ粒子は開発できるか、の４点である。

まず１に関して、C26マウス大腸癌細胞を1匹

あたり1 x 10^6細胞をBLAB/cマウスに皮下移植したモデルを用いて検証を行った。まず分子量200万Daの蛍光標識デキストランを用いて、TGF-β阻害の効果を検討した。また、PEG化リポソーム内包アドリアマイシン（ドキシル®）8mg/kgをTGF-β阻害剤と併用して投与する方法の効果を検討した。TGF-β阻害剤の投与量は1mg/kgをナノ粒子と同時腹腔内投与とした。

次に、２に関しては、リンパ管新生促進増殖因子であるVEGF-Cを吸着する可溶性VEGFR3のレンチウイルス発現コンストラクトを作成し、可溶性VEGFR3安定発現ヒト膵癌細胞(BxPC3)株を樹立、この細胞株をBALB/c nudeマウス（以下ヌードマウス）への皮下移植することにより、リンパ管の減少を伴う腫瘍モデルを樹立した。これに前述のドキシルをTGF-β阻害剤と併用して投与した。また、ヒトスキルス胃癌細胞株OCUM-2MLNは、ヌードマウス胃壁に同所移植した場合、大量の腫瘍内リンパ管新生を惹起し、所属リンパ節への転移を起こす。この系を用いて、消炎鎮痛剤であるCOX2阻害剤を投与することにより、リンパ管新生の制御が可能であるかどうかを検討した。

３に対して、ヒト胆管細胞癌細胞株OCUG-1などのヌードマウス移植モデルを、組織学的に、及び2MDaデキストランにより生理学的に検討した。

4に対しては、分担研究者西山が白金製剤であるDACHPtを内包するミセルをPEG-P(Glu)の組成を変化させ、体内動態と制ガン活性評価をマウス大腸癌C26細胞株皮下移植モデルにて行った。

倫理面では、動物実験に関して、所属機関の規則を遵守し動物愛護の観点から適切に行った。

C．研究結果

１に関して、C26皮下移植モデルに投与した分子量200万Daの蛍光標識デキストランは、コントロールですでに多量に腫瘍内分布があり、TGF-β阻害剤併用によっても有意な増強をもたらさなかった。さらに、ドキシルも単剤で十分な腫瘍増殖抑制効果があり、TGF-β阻害剤併用により差はなかった。すなわち、TGF-β阻害剤の効果は、元から漏出性が十分である血管壁に対しては、漏出効果の効果増強を及ぼさないことが示された。

２に関し、可溶性VEGFR3安定発現モデル（リンパ管減少モデル）では、ドキシルをTGF-β阻害剤と併用投与することにより、薬剤蓄積量の増加傾向を確認した。また、ヒトスキルス胃癌細胞株OCUM-2MLN同所移植モデルでは、消炎鎮痛剤であるCOX2阻害剤を投与したところ、リンパ管新生が減少し、所属リンパ節転移が減少することが観察された(Iwata C et al, Cancer Res. 67 (21):10181-10189 (2007))。このモデルも用いて、今後ナノ粒子の蓄積増減を検討する予定である。

３に対しては、ヒト胆管細胞癌細胞株およびヒトスキルス胃癌皮下移植モデルを検討した結果、実際のヒト難治腫瘍と比較して、血管密度はより高く、また腫瘍間質の線維化ははるかに少なく、すなわち組織構築に大きな隔たりがあることが判明した。つまり難治腫瘍由来の細胞であるにもかかわらず、組織型的には難治癌の特徴を備えていないことが示された。

4では、まずDACHPt内包ミセルの体内動態は、24時間後において投与量の16%が血中に滞留し、固形腫瘍に効果的に集積することが確認され、中

でもPEG-P(Glu)12-20から形成されるミセルによって最も高いガン選択性が達成された。また、C26モデルでの抗腫瘍活性は、4または6 mg/kg×4の投与量で有意であった。一方、DACHPt内包ミセルは4回投与によって最大で20%以下の体重減少を示したが、すべての個体で体重回復し、致死性の毒性は認められなかった。このミセルに蛍光物質Alexa488の付加が可能であることが示された。

D．考察

1に関して、TGF-β阻害剤の効果は、血管壁漏出性が十分でない血管に対して、それを増強させる効果であり、元来漏出性が十分である血管壁に対しては、効果増強を及ぼさないことが示された。これにより、当治療法の適応可能範囲を絞り込むのに重要な情報となった。2について、リンパ管新生の抑制は、EPR効果をさらに増強する可能性が示唆された。3に関しては、簡便さからマウス皮下移植系はそのまま用いるとしても、薬剤が血管から漏出して腫瘍間質を通過し、腫瘍細胞の集団に到達して初めて奏効するという、腫瘍における薬剤送達を研究するモデルとしては、より妥当な系の確立の必要が考えられた。4に関しては、有意な制ガン活性が確認されているDACHPt内包ミセルに関して、ミセルを構成するPEG-P(Glu)ブロック共重合体の組成の最適化を行うことで肝臓や脾臓に対する集積を抑え、ガン選択性に優れたDACHPt内包ミセルが構築できることが明らかとなった。またトレーサー機能については蛍光標識したDACHPt内包ミセルを開発することに成功し、今後の薬効評価に役立つものと考える。

E．結論

今年度の研究結果から、ヒト難治癌組織内での薬剤送達を左右する腫瘍内微小環境の研究に妥当な動物モデルの構築を、今後のより重要な課題として加えることとした。一方では、DACHPt内包ミセルを構成するPEG-P(Glu)ブロック共重合体の組成の最適化と蛍光色素の導入によりトレーサー機能の付与を行った。

F．健康危険情報

特記すべきことなし。

G．研究発表

1．論文発表

1. MR. Kano, N. Nishiyama, et al. Improvement of cancer-targeting therapy, using nanocarriers for intractable solid tumors by inhibition of TGF-β signaling. Proc. Natl. Acad. Sci. U.S.A., 104(9): 3460-3465 (2007).

2. C. Iwata, M. R. Kano, et al. Inhibition of Cyclooxygenase-2 (COX-2) Suppresses Lymph Node Metastasis via Reduction of Lymphangiogenesis. Cancer Res. 67 (21):10181-10189 (2007)

2．学会発表

1. Kano et al. Low-dose TGF-beta inhibitor improves cancer therapy using nanocarriers for intractable solid tumors. The 34th Annual Meeting of the Controlled Release Society, USA. July 7-11, 2007.

2. Kano et al, Low-dose TGF-beta inhibitor improves cancer-targeting therapy using nanocarriers for intractable solid tumors. Gordon Research Conference Angiogenesis, Newport, RI, USA. August 19-24, 2007. 他

H．知的財産権の出願・登録状況

特許取得

・宮園浩平、片岡一則、狩野光伸、ベーユンスー、西山伸宏、平川弘聖、八代正和、野出學、TGF-βシグナル阻害剤と抗腫瘍剤の組合せ使用 (PCT/JP2006/317593)

・片岡一則、熊谷康顕、狩野光伸、関野正樹、松浦哲也、西山伸宏、宮園浩平：腫瘍撮像用MRI造影剤、特願2007-124908

別添 4

厚生労働科学研究費補助金（医療機器開発推進研究事業）
分担研究報告書

がん微小環境制御を併用したナノドラッグによる難治性固形がん治療の実現
（白金錯体制ガン剤 DACHPt を内包した高分子ミセルの構築）

主任研究者　西山伸宏　東京大学大学院医学系研究科臨床医工学部門　講師

研究要旨

本研究では、難治ガンの標的治療を目的として、高分子ミセル型ナノキャリアの最適化と高機能化を目指している。本年度は、白金錯体制ガン剤である DACHPt を内包した高分子ミセルを構築し、その基本性能の検証を行った。高分子ミセルを構成するブロック共重合体の組成を最適化することによって、固形ガンに効果的に集積し、優れた抗腫瘍効果を示すことが明らかとなった。

A．研究目的

本研究では、上記の高分子ミセル型ナノドラッグを研究代表者である狩野に供給し、新しい治療戦略に基づいて難治性固形ガンの標的治療を実現することを目指している。本年度は、白金錯体制ガン剤である dichloro (1,2- diaminocyclohexane) platinum(II)(DACHPt)(オキサリプラチンの中間活性体)を内包した高分子ミセルに関して、ブロック共重合体の組成の最適化を行い、固形ガンへの集積性ならびに制ガン活性を評価した。

B．研究方法

1. DACHPt 内包ミセルの調製

本研究では、ミセル調製に用いるブロック共重合体として、ポリエチレングリコール-ポリグルタミン酸ブロック共重合体(PEG-P(Glu))を用いた。PEG-P(Glu)は、ω末端にアミノ基を有するポリエチレングリコール(PEG-NH_2:分子量 12,000)を開始剤として、γ-ベンジル-L-グルタメート *N*-カルボン酸無水物(BLG-NCA)を 40℃、DMF 中で開環重合し、得られた PEG-PBLA を 0.5N NaOH 水溶液中で加水分解することによって調製した。本研究では、P(Glu)の重合度が異なる 3 種類の組成の PEG-P(Glu)を合成したが、^{1}H-NMR ならびに GPC 解析によって、得られたブロック共重合体の P(Glu)の重合度は 20, 40, 70 であり、非常に狭い分子量分布(Mw/Mn が 1.1 以下)を有することが確認された(以下、得られた組成を 12-20, 12-40, 12-70 と表記する)。DACHPt 内包ミセルは、DACHPt に水中で硝酸銀($AgNO_3$)を作用させ、塩化銀の沈殿をフィルターを用いて除去することによって、DACHPt を活性化(アコ錯体化)した後に、PEG-P(Glu)と水中で 120 時間、錯体形成させることによって、調製した。調製した DACHPt 内包ミセルの精製は、限外ろ過によって行い(分画分子量:10 万)、高分子ミセルの粒子径を動的光散乱

(DLS)によって測定した。その結果、ダハプラチン内包高分子ミセルは、30-40nm の平均粒径と非常に狭い粒径分布を有していることが確認された。

2. DACHPt 内包ミセル体内動態と制ガン活性評価

体内動態試験: CDF1 マウス(雌,n=6)の皮下にマウス大腸癌 C-26 細胞(1×10^6)を移植し、14 日後にダ DACHPt 内包ミセルおよびオキサリプラチンを尾静脈より全身投与した。一定時間後に、血液およびガンを採取し、ホモジナイズ、5N 硝酸中での加熱処理後に、2N 塩酸に溶解し、ICP-MS により白金量を定量した。制ガン活性試験: CDF1 マウス(雌,n=6)の皮下に C-26 細胞(1×10^6)を移植し、7 日後から 2 日おきに 4 回 DACHPt 内包ミセルおよびオキサリプラチンを尾静脈より投与した。その治療効果、副作用は、それぞれ腫瘍体積変化および体重変化を経時的に測定することにより評価した。

（倫理面への配慮）

本研究では、動物実験に関して「動物の保護および管理に関する法律」などに従い、動物愛護の観点に十分に配慮して実験を行った。

C．研究結果

1. DACHPt 内包ミセルの体内動態評価

オキサリプラチンは血中より速やかに消失したが、12-40 から形成された DACHPt 内包ミセルは、血流中を長期滞留し(24 時間後において投与量の 16%が滞留)、固形ガンに効果的に集積することが確認された。また、血中 AUC を算出したところ、DACHPt 内包ミセルははオキサリプラチンの 484 倍(24 時間後)、540 倍(48 時間後)の血中 AUC を有することが確認された。次に、異なる組成の PEG-P(Glu)から形成される DACHPt 内包ミセルに関して、24 時間後のガンと正常組織の集積比を算出した結果、DACHPt 内包ミセルは肝臓、脾臓、腎臓の全てに関してガン選択的な集積を示したが、PEG-P(Glu)12-20 から形成される高分子ミセルによって最も高いガン選択性が達成された。

2. DACHPt 内包ミセルの制ガン活性

前述の PEG-P(Glu)12-20 から形成される DACHPt 内包ミセルのマウス大腸ガン C-26 細胞の皮下移植モデルに対する抗腫瘍効果を評価した結果、オキサリプラチン単独投与群では治療効果が見られなかったが、DACHPt 内包ミセルは、すべての投与量(4, 6 mg/kg×4)において有意な制ガン活性を示した。一方で、DACHPt 内包ミセルは 4 回目の投与によって最大で 20%以下の体重減少を示したが、すべてのマウスにおいて体重が回復し、致死性の毒性は認められなかった。

D．考察

本研究では、血中滞留性に優れた高分子ミセル型 DDS(ナノドラッグ)を研究代表者である狩野に供給し、新しい治療戦略に基づいて難治性固形ガンの標的治療を実現することを目指している。本年度は、既に優れた血中滞留性と腫瘍選択的な集積性、ならびに有意な制ガン活性が確認されている DACHPt 内包ミセルに関して、ミセルを構成する PEG-P(Glu)ブロック共重合体の組成の最適化を行った。その結果 12-20 の組成(X-Y: X: PEG の分子量×10^{-3}; Y: polymerization degree of P(Glu))を用いることによって、肝臓や脾臓に対する集積を抑え、ガン

選択性に優れた DACHPt 内包ミセルが構築できることが明らかとなった。DACHPt 内包ミセルは、マウスに致死性の毒性を示すことなく、オキサリプラチンに感受性の低い C-26 の皮下移植モデルに対しても有意な制ガン活性を示すことが明らかとなった。したがって、今後は、最適化された DACHPt 内包ミセルを用いて、狩野との連携により難治性ガンに対する新しい治療戦略を開発する予定である。このような研究においては、腫瘍組織内における DDS の分布を可視化することが必要であるものと考えられるが、この点においては本年度に PEG-P(Glu)に Alexa488 を導入することによって蛍光標識した DACHPt 内包ミセルを開発することに成功しており、狩野との連携においては蛍光標識 DACHPt 内包ミセルを用いることを計画している。

E．結論

本年度は、DACHPt 内包ミセルを構成する PEG-P(Glu)ブロック共重合体の組成の最適化を行い、腫瘍集積性に優れたミセル型 DDS を構築した。DACHPt 内包ミセルにトレーサーとして蛍光色素を導入することにも成功しており、今後は、研究代表者である狩野との連携により難治性ガンに対する新しい治療戦略を開発する予定である。

G．研究発表

1. 論文発表

H. Cabral, N. Nishiyama, K. Kataoka, Optimization of (1,2-diamino-cyclohexane) platinum(II)-loaded polymeric micelles directed to improved tumor targeting and enhanced antitumor activity. J. Control. Release 121 (3) 146-155 (2007)

Y. Bae, N. Nishiyama, K. Kataoka, In Vivo Antitumor Activity of the Folate -Conjugated pH-Sensitive Polymeric Micelle Selectively Releasing Adriamycin in the Intracellular Acidic Compartments. Bioconjugate Chem. 18(4) 1131-1139 (2007)

M. R. Kano, Y. Bae, C. Iwata, Y. Morishita, M. Yashiro, M. Oka, T. Fujii, A. Komuro, K. Kiyono, M. Kamiishi, K. Hirakawa, Y. Ouchi, N. Nishiyama, K. Kataoka, K. Miyazono, Improvement of cancer-targeting therapy, using nanocarriers for intractable solid tumors by inhibition of TGF-beta signaling. P. Natl. Acad. Sci. USA. 104 (9) 3460-3465 (2007)

2. 総説

西山伸宏、片岡一則：人工ウイルスの実現に向けた高分子ミセル型ベクターの設計、細胞工学　27 (1) 56-61 (2008)

西山伸宏、片岡一則：ドラッグデリバリーシステム(DDS)と血管、血管医学　8 (3) 313-317 (2007)

西山伸宏、片岡一則：先端医療のためのインテリジェント型高分子ミセルの設計、高分子　56 (9) 736-739 (2007)

西山伸宏、片岡一則：分子標的治療薬と DDS の融合とのその可能性、ゲノム医学　7 (2) 59 (135)-62(138) (2007)

西山伸宏、片岡一則：高分子ミセルを利用したがん標的治療、Mebio Oncology,松村保広編、メジカルレビュー社　東京　(2007) 18-26

3. 学会発表

Nobuhiro Nishiyama, Kazunori Kataoka, "Design of functional drug delivery system based on polymer assemblies", **10th European Symposium on Controlled Drug Delivery (ESCDD)**, Noordwijk an Zee, The Netherlands, April 2, 2008 **(Invited Lecture)**

Nobuhiro Nishiyama, Kazunori Kataoka, "Development of smart nanocarriers for targeting therapy", **2007 International Symposium on Nano-Bioscience**, Kyung Hee University, Seoul, Korea, August 20, 2007 **(Invited Lecture)**

Nobuhiro Nishiyama, Kazunori Kataoka, "Stimuli-responsive drug and gene nanocarriers based on supramolecular assemblies", **34th Annual Meeting & Exposition of the Controlled Release Society (CRS)**, Long Beach, California, July 11, 2007 **(Invited Lecture)**

西山伸宏, "トランスレーショナルリサーチの実現に向けた高分子ミセル型 DDS の開発", **創剤フォーラム第 13 回若手研究会**, 摂南大学大阪センター, 2007 年 12 月 8 日(招待講演)

西山伸宏, 片岡一則, "高分子集合体を基盤とする薬剤・遺伝子送達キャリアの創製", **ナノ学会　第 5 回大会**, つくば国際会議場(エポカルつくば), 2007 年 5 月 23 日(招待講演)

H．知的財産権の出願・登録状況

1. 片岡一則、ジャン　ミンゼン、石井篤史、西山伸宏、松本悟：ポリエチレングリコールの結合した核酸のコンジュゲートとリン酸カルシウムの有機-無機ハイブリッド型ナノ粒子、特願 2007-280803

2. 片岡一則、熊谷康顕、狩野光伸、関野正樹、松浦哲也、西山伸宏、宮園浩平：腫瘍撮像用 MRI 造影剤、特願 2007- 124908

別添５

研究成果の刊行に関する一覧表

書籍　該当なし

雑誌

発表者氏名	論文タイトル名	発表誌名	巻号	ページ	出版年
M. R. Kano, Y. Bae, C. Iwata, Y. Morishita, M. Yashiro, M. Oka, T. Fujii, A. Komuro, K. Kiyono, M. Kaminishi, K. Hirakawa, Y. Ouchi, N. Nishiyama, K. Kataoka, and K. Miyazono.	Improvement of cancer-targeting therapy, using nanocarriers for intractable solid tumors by inhibition of TGF-β signaling.	Proc. Natl. Acad. Sci. U.S.A.	104(9)	3460-3465	2007
C. Iwata, M. R. Kano, A. Komuro, M. Oka, K. Kiyono, E. Johansson, Y. Morishita, M. Kaminishi, M. Yashiro, K. Hirakawa, and K. Miyazono.	Inhibition of Cyclooxygenase-2 (COX-2) Suppresses Lymph Node Metastasis via Reduction of Lymphangiogenesis.	Cancer Res.	67 (21)	10181-10189	2007
H. Cabral, N. Nishiyama, K. Kataoka.	Optimization of (1,2-diamino-cyclohexane) platinum(II)-loaded polymeric micelles directed to improved tumor targeting and enhanced antitumor activity.	J. Control. Release	121 (3)	146-155	2007
Y. Bae, N. Nishiyama, K. Kataoka	In Vivo Antitumor Activity of the Folate - Conjugated pH-Sensitive Polymeric Micelle Selectively Releasing Adriamycin in the Intracellular Acidic Compartments.	Bioconjugate Chem.	18(4)	1131-1139	2007
狩野光伸	ナノ粒子抗癌剤と低用量 TGF-β 阻害剤の併用による難治癌治療.	実験医学	25(9)	1344-1347	2007
狩野光伸	TGF-β シグナルの制御と癌治療.	細胞	39(8)	31-33	2007

狩野光伸・宮園浩平	血管における TGF-βファミリーシグナル	医学のあゆみ	223(12)	1037-1042	2008
西山伸宏、片岡一則	人工ウイルスの実現に向けた高分子ミセル型ベクターの設計	細胞工学	27 (1)	56-61	2008
西山伸宏、片岡一則	ドラッグデリバリーシステム(DDS)と血管	血管医学	8 (3)	313-317	2007
西山伸宏、片岡一則	先端医療のためのインテリジェント型高分子ミセルの設計	高分子	56 (9)	736-739	2007
西山伸宏、片岡一則	分子標的治療薬と DDS の融合とのその可能性	ゲノム医学	7 (2)	59 (135)-62(138)	2007
西山伸宏、片岡一則	高分子ミセルを利用したがん標的治療	Mebio Oncology	4 (2)	18-26	2007

Improvement of cancer-targeting therapy, using nanocarriers for intractable solid tumors by inhibition of TGF-β signaling

Mitsunobu R. Kano*†‡, Younsoo Bae‡§, Caname Iwata*¶, Yasuyuki Morishita*, Masakazu Yashiro‖, Masako Oka*, Tomoko Fujii*, Akiyoshi Komuro*, Kunihiko Kiyono*, Michio Kaminishi¶, Kosei Hirakawa‖, Yasuyoshi Ouchi†, Nobuhiro Nishiyama§**, Kazunori Kataoka‡§**††, and Kohei Miyazono*‡‡

Departments of *Molecular Pathology, †Geriatrics, ¶Gastrointestinal Surgery, and §Center for Disease Biology and Integrative Medicine, Graduate School of Medicine; **Department of Materials Engineering, Graduate School of Engineering; and ‡Center for Nano-Bio Integration, University of Tokyo, Tokyo 113-0033 Japan; and ‖Department of Surgical Oncology, Osaka City University Graduate School of Medicine, Osaka 545-8585, Japan

Communicated by Tadatsugu Taniguchi, University of Tokyo, Tokyo, Japan, December 28, 2006 (received for review December 25, 2006)

Transforming growth factor (TGF)-β plays a pivotal role in regulation of progression of cancer through effects on tumor microenvironment as well as on cancer cells. TGF-β inhibitors have recently been shown to prevent the growth and metastasis of certain cancers. However, there may be adverse effects caused by TGF-β signaling inhibition, including the induction of cancers by the repression of TGF-β-mediated growth inhibition. Here, we present an application of a short-acting, small-molecule TGF-β type I receptor (TβR-I) inhibitor at a low dose in treating several experimental intractable solid tumors, including pancreatic adenocarcinoma and diffuse-type gastric cancer, characterized by hypovascularity and thick fibrosis in tumor microenvironments. Low-dose TβR-I inhibitor altered neither TGF-β signaling in cancer cells nor the amount of fibrotic components. However, it decreased pericyte coverage of the endothelium without reducing endothelial area specifically in tumor neovasculature and promoted accumulation of macromolecules, including anticancer nanocarriers, in the tumors. Compared with the absence of TβR-I inhibitor, anticancer nanocarriers exhibited potent growth-inhibitory effects on these cancers in the presence of TβR-I inhibitor. The use of TβR-I inhibitor combined with nanocarriers may thus be of significant clinical and practical importance in treating intractable solid cancers.

angiogenesis | gastric cancer | molecular targeting therapy | pancreatic cancer

Chemotherapy that uses nanocarriers has been developed to improve the clinical treatment of solid tumors by obtaining high accumulation of drugs in tumor tissues but limited accumulation in normal organs. Doxil (1), a liposomal adriamycin (ADR), is one such drug that has already been used clinically (2). Doxil has exhibited therapeutic effects on some cancers with hypervascular characteristics (3, 4), including Kaposi sarcoma and ovarian cancers. Another promising formulation of nanocarriers is polymeric micelles (5, 6), which are already being used in clinical trials (7, 8).

However, despite the urgent need for effective chemotherapy for intractable solid tumors, including pancreatic adenocarcinoma (9) and diffuse-type gastric carcinoma (10), nanocarriers of any design have not been successful yet in exhibiting significant therapeutic effects on these cancers. Pancreatic cancer is the fourth leading cause of cancer-related death in the United States and the fifth in Japan (9), and the median survival period of patients who suffer from advanced pancreatic adenocarcinoma is still extremely short (≈6 months), despite recent progress in development of conventional chemotherapies (11). Although cancer cells derived from these tumors are sufficiently sensitive *in vitro* to conventional anticancer agents such as ADR (12), most of these agents have failed to exhibit sufficient therapeutic effects *in vivo*, regardless of formulation, whether encapsulated in nanocarriers or not. The theoretical basis of the specific accumulation of nanocarriers in tumor tissues is leakiness of tumor vessels to the macromolecular agents, termed the "enhanced permeability and retention (EPR) effect," which was demonstrated and named by Maeda *et al.* (13, 14). The major obstacles to treatment of these cancer cells could thus be insufficient EPR effect because of certain characteristics of their cancer microenvironment, including hypovascularity and thick fibrosis (15, 16). However, methods of regulating this effect have not been well investigated.

Transforming growth factor (TGF)-β signaling plays a pivotal role in both the regulation of the growth and differentiation of tumor cells and the functional regulation of tumor interstitium (17). Because TGF-β is a multifunctional cytokine that inhibits the growth of epithelial cells and endothelial cells and induces deposition of extracellular matrix, inhibition of TGF-β signaling in cancer cells and fibrotic components has been expected to facilitate the effects of anticancer therapy. TGF-β binds to type II (TβR-II) and type I receptors (TβR-I), the latter phosphorylates Smad2 and −3. Smad2 and −3 then form complexes with Smad4, translocate into the nucleus, and regulate the transcription of target genes (18). Several small-molecule TβR-I inhibitors have been reported to prevent metastasis of some cancers (19). However, there may be adverse effects of TGF-β inhibition, including potential progression of some cancers because of the repression of TGF-β-mediated growth inhibition of epithelial cells (20).

In this study, we show that administration of the small-molecule TβR-I inhibitor (LY364947) (21) at a low dose, which could minimize the potential side effects of TβR-I inhibitor, can alter the tumor microenvironment and enhance the EPR effect. This effect of low-dose TβR-I inhibitor was demonstrated with two of nanocarriers, i.e., Doxil and a polymeric micelle incorporating ADR (micelle ADR) that we have recently developed (22) [supporting information (SI) Fig. 7]. The present findings strongly suggest that our method, which uses a combination of

Author contributions: M.R.K., K. Kataoka, and K.M. designed research; M.R.K., Y.B., C.I., Y.M., M.O., T.F., A.K., and K. Kiyono performed research; M.Y. and K.H. contributed new reagents/analytic tools; M.R.K., Y.B., C.I., M.K., Y.O., N.N., K. Kataoka, and K.M. analyzed data; and M.R.K., N.N, K. Kataoka, and K.M. wrote the paper.

The authors declare no conflict of interest.

Freely available online through the PNAS open access option.

Abbreviations: ADR, adriamycin; EPR, enhanced permeability and retention; PECAM, platelet/endothelial cell adhesion molecule; TβR-I, type I transforming growth factor β receptor.

††To whom correspondence may be addressed at: Department of Material Engineering, Graduate School of Engineering, University of Tokyo, Tokyo 113-8656, Japan. E-mail: kataoka@bmw.t.u-tokyo.ac.jp.

‡‡To whom correspondence may be addressed. E-mail: miyazono-ind@umin.ac.jp.

This article contains supporting information online at www.pnas.org/cgi/content/full/0611660104/DC1.

www.pnas.org/cgi/doi/10.1073/pnas.0611660104

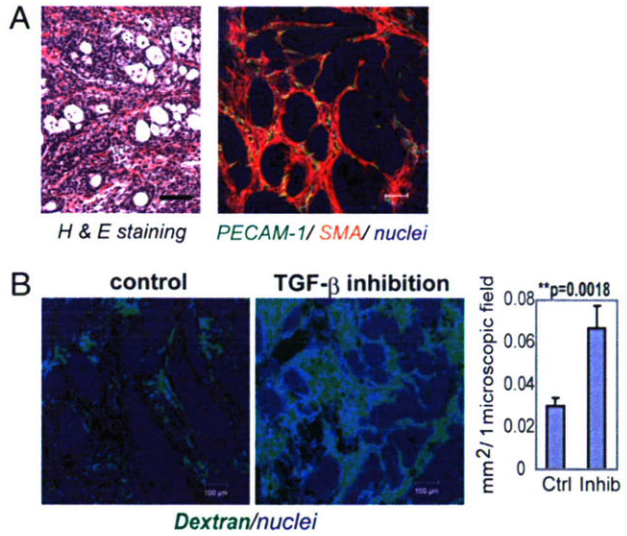

Fig. 1. Histology of BxPC3 xenograft and effects of low-dose TβR-I inhibitor. (*A*) The histology of the TGF-β-nonresponsive BxPC3 xenograft, used as a model of poorly differentiated pancreatic adenocarcinoma, shown in H&E staining and immunohistochemistry. Examination revealed nests of tumor cells in gland-like structures, with areas rich in fibrotic components (filled by α-smooth muscle actin (SMA)-positive myofibroblasts, shown in red) between them. The tumor tissue also includes some PECAM-1-positive vessels (shown in green) in the interstitium, although almost no vasculature was observed inside the nests of tumor cells. (*B*) Dextran leakage. At 24 h after administration of low-dose TβR-I inhibitor (1 mg/kg i.p.), i.v.-administered dextran of 2 MDa (50 nm in hydrodynamic diameter) exhibited broader distribution with 1 mg/kg TβR-I inhibitor (*Right*) than in the control (*Left*), which was quantified and shown in the graph ($n = 12$). Error bars in the graphs represent standard errors, and *P* values were calculated by Student's *t* test. Ctrl, control; Inhib, inhibitor. (Scale bars, 100 μm.)

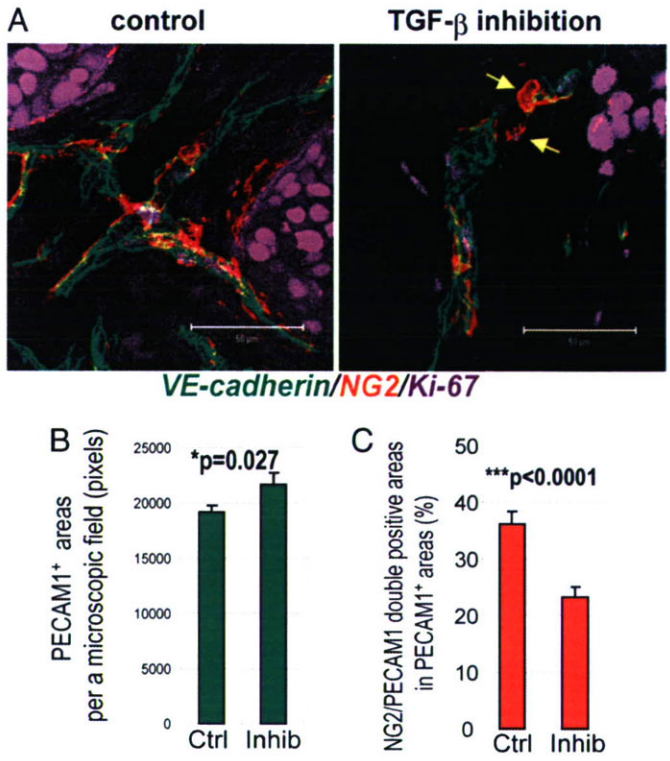

Fig. 2. Morphological changes in cancer neovasculature at 24 h after administration of low-dose TβR-I inhibitor. (*A*) Immunostaining of the tumor neovasculature. NG2-positive pericytes (shown in red) were dissociated (yellow arrows in *Right*) from VE-cadherin-positive endothelium (shown in green) after TβR-I inhibitor treatment for 24 h. (Scale bars, 50 μm.) (*B* and *C*) Areas of PECAM-1-positive endothelium (*B*) and pericyte-coverage (*C*) were quantified ($n = 40$) and are shown in the graphs. Error bars in the graphs represent standard errors, and *P* values were calculated by Student's *t* test. Ctrl, control; Inhib, inhibitor.

low-dose small molecule TβR-I inhibitor and long-circulating nanocarriers, is a promising way to treat intractable cancers.

Results

We used the xenografted BxPC3 human pancreatic adenocarcinoma cell line in nude mice as a disease model (Fig. 1). BxPC3 cells do not respond to TGF-β, because of lack of functional Smad4. Hematoxylin/eosin (H&E) staining of tumor tissue in this model (Fig. 1*A Left*) revealed poorly differentiated histology, with a certain number of blood vessels and thick fibrotic tissue in the interstitium. There was, however, almost no vasculature inside of tumor cell nests (Fig. 1*A Right*). This model thus represents the histological characteristics of some intractable solid tumors.

Systemic administration of low-dose TβR-I inhibitor in this model significantly altered the characteristic of tumor vasculature at 24 h after administration. We investigated the functional aspects of the effects of low-dose TβR-I inhibitor, using i.v.-administered large-molecule dextran of 2 MDa with a hydrodynamic diameter of 50 nm (23, 24), which is equivalent to the common sizes of nanocarriers (Fig. 1*B*). Although dextran of this molecular size for the most part remained in the intravascular space in the control condition, as reported in ref. 24, the use of TβR-I inhibitor resulted in a far broader distribution of this macromolecule around the tumor neovasculature. These findings suggest that low-dose TβR-I inhibitor can maintain blood flow in the tumor vasculature and simultaneously induce extravasation of macromolecules.

To investigate the mechanisms of effect of TβR-I inhibitor on the neovasculature, we analyzed the changes in three major components of tumor vasculature, i.e., endothelium, pericytes (Fig. 2), and basement membrane (SI Fig. 8), at 24 h after administration of TβR-I inhibitor. The areas of vascular endothelial cells stained by platelet/endothelial cell adhesion molecule (PECAM)-1 increased slightly with TβR-I inhibitor treatment (Fig. 2*B*). Although pericyte-coverage of endothelium has been reported to be incomplete in tumors (25), coverage of the endothelium by pericytes, which were determined as NG2-positive perivascular cells, was further decreased by the TβR-I inhibitor treatment. This finding was confirmed by comparing the ratios of PECAM-1/NG2-double-positive areas to PECAM-1-positive areas (Fig. 2*C*). On the other hand, vascular basement membrane, which was determined by staining with collagen IV, did not differ significantly in the presence or absence of TβR-I inhibitor (SI Fig. 8). We also examined the vasculature in normal organs and found that it was not affected by TβR-I inhibitor in terms of permeability of 2-MDa dextran and morphology on immunostaining (SI Fig. 9).

We next examined the effects of i.p. administration of small-molecule TβR-I inhibitor at a low dose (1 mg/kg) on TGF-β signaling, by determining phosphorylation of Smad2 (SI Figs. 10 and 11). Because it is a small-molecule agent, TβR-I inhibitor transiently suppressed phosphorylation of Smad2. In nucleated blood cells, phosphorylation of Smad2 was significantly suppressed at 1 h after administration of TβR-I inhibitor, but it gradually recovered toward 24 h. In contrast, phosphorylation of Smad2 in tumor cells and most interstitial cells was not suppressed even 1 h after administration, whereas a higher dose (25 mg/kg) of TβR-I inhibitor inhibited Smad2 phosphorylation in most tumor cells. Accordingly, the extent of fibrosis in cancer xenografts treated with low-dose TβR-I inhibitor did not differ

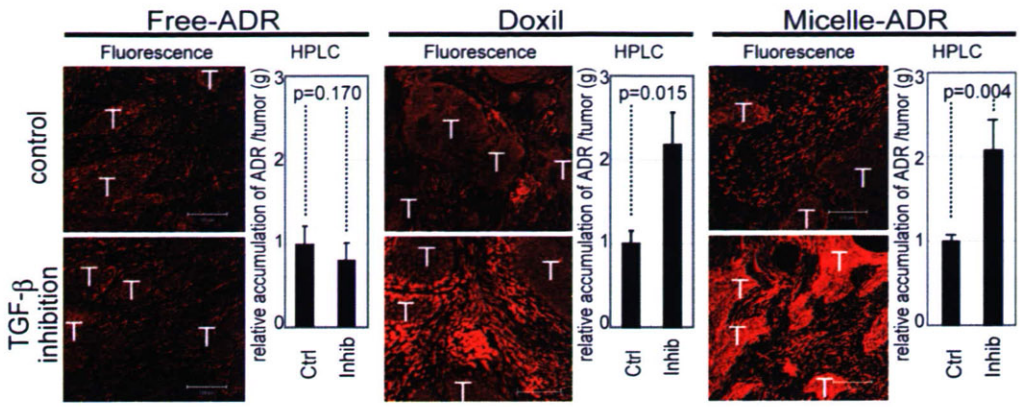

Fig. 3. Biodistribution of ADR in the BxPC3 model. The biodistribution of ADR was investigated in the BxPC3 model by fluorescence examination (T indicates nests of tumor cells in tumor tissues) and by HPLC. The distributions of Doxil, micelle ADR, and free ADR at 8 mg/kg with and without TβR-I inhibitor at 1 mg/kg were examined 24 h after administration. Enhancement of drug accumulation in tumor was specifically observed with TβR-I inhibitor with Doxil and micelle ADR. Error bars in the graphs represent standard errors, and *P* values were calculated by Student's *t* test. Ctrl, control; Inhib, inhibitor.

from that in the control (SI Fig. 12). On the other hand, low-dose TβR-I inhibitor specifically suppressed the phosphorylation of Smad2 in vascular endothelium (SI Fig. 11*B*). These findings suggest that the use of small-molecule TβR-I inhibitor at low doses is advantageous for limiting adverse effects.

We thus hypothesized that low-dose TβR-I inhibitor may enhance the accumulation of nanocarriers, the molecular sizes of which are similar to 2-MDa dextran, in hypovascular solid tumors. We used two nanocarriers to test this hypothesis: Doxil (26), a liposomal ADR, and a core–shell type polymeric micelle-encapsulating ADR (micelle ADR) that we developed (22). The latter is a micellar nanocarrier consisted of block copolymers in which ADR is conjugated to the PEG chain through an acid–labile linkage. This drug carrier releases free ADR molecules selectively in acidic conditions, e.g., in intracellular endosomes and lysosomes (SI Fig. 7). We tested the effects of i.p. administration of TβR-I inhibitor with i.v. administration of Doxil or micelle ADR at 8 mg/kg on size-matched xenografts of BxPC3 cells, which are ADR-sensitive *in vitro* (12). Conventional ADR without drug carriers (free ADR), a small-molecule compound of MW 543.52, was also used for comparison. We first examined the distribution of ADR molecules in tumor tissues by using confocal imaging of fluorescence of ADR and HPLC (Fig. 3). The fluorescence of ADR molecules in micelle ADR is detectable only when ADR molecules are released from the micelle, whereas that in Doxil is detectable even when it is encapsulated in the liposome. The total amount of accumulated ADR, the sum of that in cancer cells and the cancer microenvironment, is measured by HPLC, which detects ADR molecules with and without drug carriers. Administration of TβR-I inhibitor with the nanocarriers yielded significant enhancement of intratumoral accumulation of ADR molecules. Because TβR-I inhibitor did not increase the accumulation of free ADR, we suspected that only macromolecules would be benefited by the use of TβR-I inhibitor through enhancement of EPR effect.

We then examined the growth-inhibitory effects of these anticancer drugs with and without TβR-I inhibitor on size-matched BxPC3 xenografts. As shown in Fig. 4*A*, the growth curves of the BxPC3 xenografts confirmed the findings for the distribution of ADR molecules. None of free ADR, Doxil, micelle ADR as monotherapy, or free ADR with TβR-I inhibitor significantly reduced tumor growth. In contrast, ADR encapsulated in nanocarriers exhibited significant effects on the growth of tumor when combined with TβR-I inhibitor (see *SI List* for statistical study).

Because micelle ADR was more effective than Doxil (as shown in Figs. 3 and 4*A*), and the maximum tolerated dose of micelle ADR is far higher than one shot of 8 mg/kg (22, 26) (the dose in Fig. 4*A*), we further tested the growth-inhibitory effects of an increased dose of micelle ADR combined with TβR-I inhibitor (Fig. 4*B*). When micelle ADR or free ADR was

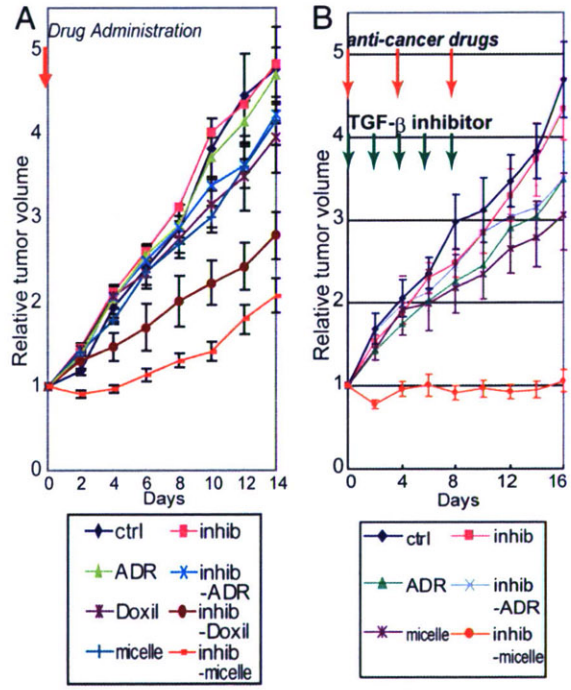

Fig. 4. Effects of TβR-I inhibitor on anti-tumor activity of nanocarriers, incorporating ADR in the BxPC3 model. (*A*) Free ADR, liposomal ADR (Doxil), micelle ADR (micelle) or vehicle control (ctrl) was administered i.v. in a single bolus with and without TβR-I inhibitor (inhib) i.p. to xenografted mice in which tumors had been allowed to grow for a few weeks before treatment ($n = 5$). Relative tumor sizes were measured every second day and are shown as a growth curve with bars showing standard errors. Only nanocarriers administered together with TβR-I inhibitor exhibited significant reduction of growth compared with the control. (*B*) Growth curve study with an increased dose of micelle ADR. With the day of initiation of drug administration designated day 0, anticancer drugs were administered i.v. on days 0, 4, and 8 with and without i.p. TβR-I inhibitor on days 0, 2, 4, 6, and 8. Further growth-inhibitory effect was observed with an increase in dose of micelle ADR. (Results of multivariate ANOVA study are shown in *SI List*.)

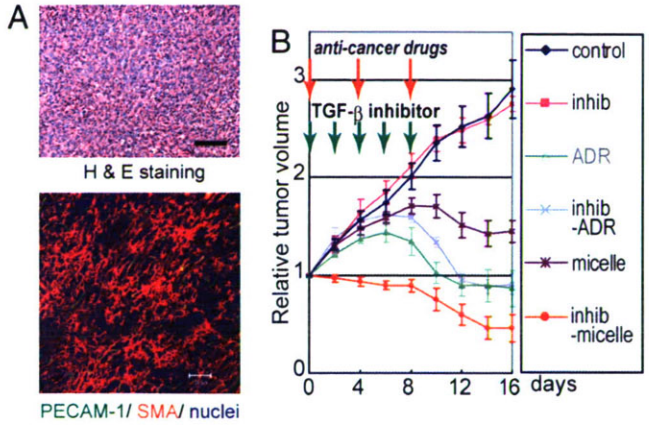

Fig. 5. Growth-curve study in the MiaPaCa-2 pancreatic cancer xenograft model. (*A*) TGF-β-nonresponsive MiaPaCa-2 cell xenografts exhibited an undifferentiated pattern of histology on H&E staining (*Upper*), with rich SMA-positive fibrotic tissue (show in red in *Lower*) and much less PECAM-1-positive vasculature (shown in green) compared with the BxPC3 model. (*B*) The same experimental protocol as in Fig. 4*B* was used in the model, and the effectiveness of the use of TβR-I inhibitor was confirmed. Inhib, inhibitor; micelle, micelle-ADR. (Results of multivariate ANOVA for the growth-curve studies are shown in *SI List*.)

administered on days 0, 4, and 8, with and without TβR-I inhibitor, only micelle ADR administered together with TβR-I inhibitor exhibited nearly complete growth-inhibitory effect on the tumor in this model. We therefore used this regimen in the following experiments.

The efficacy of combined treatment was further confirmed by using micelle ADR in two other animal models of pancreatic adenocarcinoma. We used size-matched xenograft models of MiaPaCa-2 and Panc-1 cell lines, which are both ADR-sensitive *in vitro* (12) (Fig. 5 and SI Figs. 13 and 14). MiaPaCa-2 is nonresponsive to TGF-β signaling because of TβR-II deficiency, whereas Panc-1 has no deficiency in TGF-β signaling components and responds to TGF-β. On histological examination, the xenografts of MiaPaCa-2 and Panc-1 exhibited similar undifferentiated pattern with scattered cancer cells, rich fibrous tissue, and sparse vasculature distributed homogeneously, unlike that of BxPC3 xenografts (Fig. 5*A* and SI Fig. 14*A*). Use of low-dose TβR-I inhibitor in these models again significantly enhanced the growth-inhibitory effects of micelle ADR (see Fig. 5*B*, SI Fig. 14*B*, and *SI List* for statistical analyses). Effects of free ADR were again not enhanced by TβR-I inhibitor, although the drug itself exhibited some degree of growth-inhibitory effect on the MiaPaCa-2 xenografts. Analysis of the biodistribution of ADR molecules (SI Figs. 13 and 14 *C* and *D*) confirmed the effects of TβR-I inhibitor on accumulation of micelle ADR in these cancer models.

We also tested the growth-inhibitory effect of TβR-I inhibitor and micelle ADR in an orthotopic model of the OCUM-2MLN cell line, which responds to TGF-β (27) (Fig. 6). OCUM-2MLN was derived from a patient with another intractable solid tumor, diffuse-type gastric cancer. The cancer cells were implanted in the gastric wall of nude mice and allowed to grow *in situ* for 2 weeks, leading to formation of hypovascular and fibrotic tumors in the gastric wall (Fig. 6*A*). Tumor area (framed by arrowheads in Fig. 6*B*, *Left*) was measured before the initiation of drug administration, and tumor growth was evaluated by calculating the relative tumor area at day 16 by measuring tumor area again (Fig. 6*B*, *Right*). Significant reduction of tumor growth was again observed only in the mice treated with TβR-I inhibitor and micelle ADR. The distribution of ADR, as detected by fluorescence, confirmed this growth-inhibitory effect (data not shown). These findings suggest that the use of TβR-I inhibitor may enhance the accumulation of nanocarriers in hypovascular solid tumors.

Finally, we examined whether low-dose TβR-I inhibitor increases EPR effect specifically in tumor tissues and not in normal organs. Although nanocarriers were originally designed to decrease the drug accumulation in normal organs, it is important to determine whether use of TβR-I inhibitor exacerbates their side effects (SI Fig. 15). In liver, spleen, kidney, blood, and heart, accumulation of ADR as determined by HPLC was not significantly increased by TβR-I inhibitor (SI Fig. 15 *A* and *B*). Neither dermatitis nor phlebitis around the tail veins was exacerbated by addition of TβR-I inhibitor (SI Fig. 15*C*). In addition, the weight

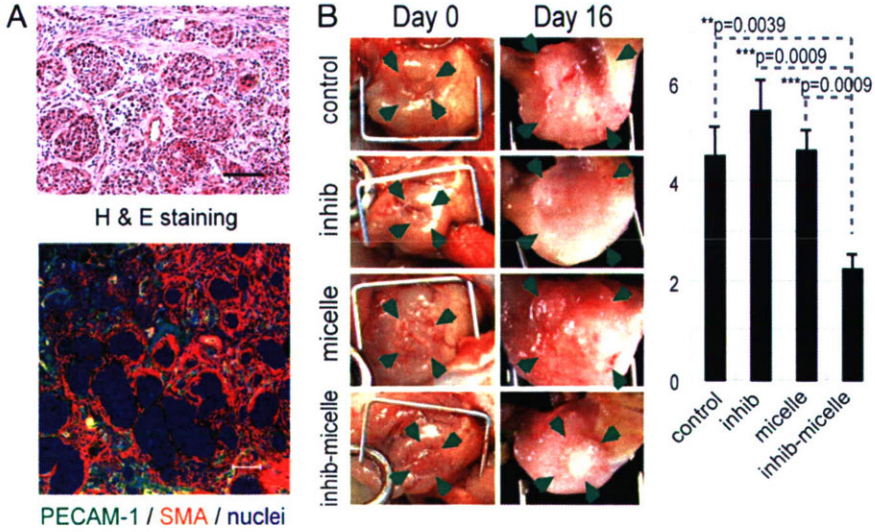

Fig. 6. Effects of TβR-I inhibitor administered together with micelle ADR in an orthotopic diffuse-type gastric cancer model. OCUM-2MLN, a human diffuse-type gastric cancer cell line, was inoculated into the gastric wall of nude mice ($n = 5$). Two weeks after inoculation, the cancer tissues exhibited diffuse-type histology on H&E staining (*A Upper*) with sparse formation of blood vessels (PECAM-1 staining, shown in green) (*A Lower*). The sizes of tumors on the gastric wall were measured based on tumor areas (*B Left*), and the values on day 16 were divided by those on day 0, the day of initiation of drug administration, to obtain relative tumor areas. Relative tumor areas are shown with bars for standard errors (*B Right*). TβR-I inhibitor significantly reduced tumor growth in this model, as well. *P* values were calculated by Student's *t* test. Inhib, inhibitor; micelle, micelle-ADR.

of mice that were treated with micelle ADR was not significantly affected by TβR-I inhibitor (data not shown). These findings in normal organs strongly suggest that low-dose TβR-I inhibitor enhances EPR effect only in tumors and that exacerbation of toxicity or side effects of nanocarrier-encapsulated drugs may be minimal with this treatment.

Discussion

In the present study, we have tested a use of TβR-I inhibitor at a low dose to induce alteration in cancer-associated neovasculature to exhibit more leakiness for macromolecules, with less pericyte-coverage and greater endothelial area (Figs. 1 and 2). Because use of TβR-I inhibitor induced the same alteration in neovasculature in the Matrigel plug assay (M.R.K., unpublished data), a model of adult neoangiogenesis (23), the effects of use of TβR-I inhibitor on tumor vasculature observed in the present study may be common in adult neoangiogenesis. Although the roles of growth factors, including TGF-β, may differ during development and in adults, these phenotypes are reminiscent of those of knockout mice deficient in certain components of TGF-β signaling, e.g., endoglin (28, 29), ALK-1 (30, 31), and ALK-5 (32), in which loss of pericyte-coverage and dilatation of the vasculature in yolk sac or embryos were observed. These phenotypes are also consistent with the findings obtained on *in vitro* culture of endothelial cell lineages (33) and mesenchymal progenitor cells (34), which showed that pericyte maturation is promoted, and endothelial proliferation is inhibited, by TGF-β signaling. Vascular phenotypes due to defects in TGF-β signaling *in vivo* are also observed in two types of hereditary hemorrhagic telangiectasia (35, 36), which are induced by deficiencies of endoglin or ALK-1, which are components of TGF-β signaling in vascular endothelium. Because of inborn and life-long abnormality of TGF-β signaling in vasculature, these diseases result in a tendency toward hemorrhage in capillaries that is due to vulnerability of the vascular structure. These observations suggest that use of TβR-I inhibitor at a dose corresponding to that in mice in our study may have similar effects in humans. However, the inhibition of TGF-β signaling is only transient in our method, because of the use of small-molecule inhibitor, and the effects of TβR-I inhibitor may thus be far less severe than the phenotypes observed in hereditary hemorrhagic telangiectasia.

The changes in tumor neovasculature induced by TβR-I inhibitor resulted in enhanced extravasation of molecules, although in a molecular-size dependent manner. Accumulation of 2-MDa dextran with a 50-nm hydrodynamic diameter, Doxil with a 108-nm diameter, and micelle ADR with a 65-nm diameter was enhanced by TβR-I inhibitor in the present study, although accumulation of small-molecule agents, including ADR (MW 543.52) and BrdU (MW 307.10) (M.R.K., unpublished data), was not significantly enhanced. Dreher *et al.* (24) recently reported the molecular-size-dependency of intratumoral drug distribution, using a xenograft model of FaDu cells derived from human hypopharyngeal squamous cell carcinoma. They used several dextrans with molecular sizes ranging from 3.3 kDa to 2 MDa, with estimated hydrodynamic diameters of 3.5 nm to 50 nm, respectively. Dextran molecules of 3.3 kDa and 10 kDa, the smallest ones tested, were found to penetrate deeply and homogeneously into tumor tissue, although they remained in tumor tissue only transiently, for far less than 30 min. However, larger dextran of 2 MDa with a diameter of 50 nm, which we also used in the present study, for the most part remained in the vasculature in cancer tissue and reached only an ≈5-μm distance from the vessel wall at 30 min after injection. Although the histological characteristics of their model, which were not described in their report, may differ from those of the cancer models used in our study, the distribution of 2-MDa dextran observed by Dreher *et al.* agrees with that obtained without TβR-I inhibitor in the BxPC3 xenografts observed in the present study (Fig. 3). TβR-I inhibitor could thus enhance the accumulation of macromolecules with hydrodynamic diameters of >50 nm, common sizes for nanocarriers, in cancers other than those used in the present study. However, the range of sizes of macromolecules and histological patterns of cancer for which use of TβR-I inhibitor can exhibit enhancing effects remains to be determined.

In conclusion, we have proposed here a use of small-molecule TβR-I inhibitor at a low dose to enhance EPR effect in intractable solid cancers. This method could be a breakthrough in chemotherapy by using nanocarriers in these cancers. Because low-dose TβR-I inhibitor does not affect cancer cells, it may reduce the potential side effects of TGF-β inhibitors, and its enhancing effect is independent of the reactivity of cancer cells to TGF-β signaling. Use of TGF-β inhibitors may thus enable reduction of the systemic doses of nanocarriers and thereby decrease the adverse effects of anticancer drugs.

Methods

TGF-β Inhibitors, Anticancer Drugs, and Antibodies. TβR-I inhibitor was purchased from Calbiochem (San Diego, CA) (LY364947; catalog no. 616451). ADR was obtained from Nippon Kayaku (Tokyo, Japan) and purchased from Kyowa Hakko (Tokyo, Japan). Doxil was purchased from Alza (Mountain View, CA). Micelle ADR was prepared as reported (22) (see *SI Materials and Methods* for detailed information). The antibodies to PECAM-1 and VE-cadherin were from BD PharMingen (San Diego, CA), those to neuroglycan 2 and collagen IV were from Chemicon (Temecula, CA), and that to SMA was from Sigma–Aldrich (St. Louis, MO). The anti-phospho-Smad2 antibody was a gift from A. Moustakas and C.-H. Heldin (Ludwig Institute for Cancer Research, Uppsala, Sweden).

Cancer Cell Lines and Animals. BxPC3, MiaPaCa-2, and Panc-1 human pancreatic adenocarcinoma cell lines were obtained from the American Type Culture Collection (Manassas, VA). The OCUM-2MLN human diffuse-type gastric cancer cell line was previously established (27). BxPC3 cells were grown in RPMI medium 1640 supplemented with 10% FBS. MiaPaCa-2, Panc-1, and OCUM-2MLN cells were grown in DMEM with 10% FBS. BALB/c nude mice, 5–6 weeks of age, were obtained from CLEA Japan (Tokyo, Japan), Sankyo Laboratory (Tokyo, Japan), and Charles River Laboratories, (Tokyo, Japan). All animal experimental protocols were performed in accordance with the policies of the Animal Ethics Committee of the University of Tokyo.

Cancer Models. The effects of anticancer drugs were assessed by s.c. implantation of cancer cells into nude mice, and by orthotopic inoculation of OCUM-2MLN cells into the gastric walls of nude mice. A total of 5×10^6 cells in 100 μl of PBS for the xenograft models and the same number in 50 μl of PBS for the orthotopic model were injected into male nude mice and allowed to grow for 2–3 weeks to reach proliferative phase, before initiation of drug administration. For growth-curve studies, the day of initiation of drug administration was considered day 0, and TβR-I inhibitor, dissolved to 5 mg/ml in DMSO and diluted by 100 μl of PBS, or the vehicle control, was injected i.p. at 1 mg/kg on day 0 only in the experiment shown in Fig. 4*A* and on days 0, 2, 4, 6, and 8 in other experiments. Doxil, micelle ADR, and free ADR at 8 mg/kg, or normal saline as vehicle control, were also administered i.v. in 200 μl/vol via the tail vein on day 0 (Fig. 4*A*). In other experiments, micelle ADR at 16 mg/kg, free ADR at 8 mg/kg, or normal saline was also administered i.v. on days 0, 4, and 8. There were five mice per group per cell line. The doses of ADR and Doxil were determined based on the lethal doses in mice (22, 26). For biodistribution studies, three mice per group per cell line were treated with 8 mg/kg Doxil, micelle

ADR, or free ADR i.v., with and without TβR-I inhibitor at 1 mg/kg i.p. The mice were examined 24 h after injection.

Quantification in Tumor Models. Xenograft tumors were measured externally every second day until day 16, and tumor volume was approximated by using the equation vol = $(a \times b^2)/2$, where vol is volume, a the length of the major axis, and b is the length of the minor axis. Relative tumor volume was calculated by dividing tumor volume by that on day 0 (the day of initiation of treatment), where actual estimated volumes of xenografted tumors in mm^3 at initiation of drug administration were as follows (mean ± standard error): BxPC3 (in Fig. 4*A*), 76.4± 7.0; BxPC3 (in Fig. 4*B*), 74.4 ± 3.3; MiaPaCa-2, 221.2 ± 12.7; and Panc-1, 242.16 ± 24.5. For orthotopic OCUM-2MLN tumors, the area of the primary focus on the gastric wall was measured in Adobe Photoshop software, by opening the abdomen before initiation of treatment and at the end of the observation period. Relative tumor area was calculated by dividing tumor area by that on the day of initiation of treatment. The results were further analyzed statistically by the multivariate ANOVA test, using JMP6 software (SAS Institute, Raleigh, NC).

Histology and Immunohistochemistry. The excised samples were either directly frozen in dry-iced acetone for immunohistochemistry, or fixed overnight in 4% paraformaldehyde and then paraffin-embedded to prepare them for H&E or AZAN staining. Frozen samples were further sectioned at 10-μm thickness in a cryostat, briefly fixed with 10% formalin, and then incubated with primary and secondary antibodies. TOTO-3 for nuclear staining, Alexa488-, Alexa594-, and Alexa647-conjugated secondary antibodies, anti-rat and rabbit IgGs, Zenon labeling kit anti-rabbit and mouse IgG, and FITC-conjugated dextran (MW 2×10^6) were purchased from Invitrogen Molecular Probes (Eugene, OR). Samples were observed by using a Zeiss (Thornwood, NY) LSM510 Meta confocal microscope for immunohistochemistry, and an Olympus (Tokyo, Japan) AX80 microscope for H&E and AZAN staining.

Biodistribution. Xenografts were inoculated s.c. in nude mice and allowed to grow for 2–3 weeks before drug administration. We then injected TβR-I inhibitor at 1 mg/kg i.p. together with i.v. administration of Doxil, micelle ADR, or free ADR at 8 mg/kg. The tumors or organs were excised 24 h after injection of drugs, and frozen in dry-iced acetone to obtain fluorescence images or weighed and mixed with daunorubicin commensurate with the sample weight as an internal control and then frozen to prepare them for measurement by HPLC. The HPLC method used for analyses is described in ref. 22. To obtain fluorescence images, we performed cryostat sectioning of the frozen samples and washed the sections twice briefly with PBS but did not fix them to avoid elution of ADR. The samples were then observed with a Zeiss confocal microscope, using an excitation laser at 488 nm and a detection filter for the infrared region.

We thank Erik Johansson (University of Tokyo) for assistance. This work was supported by a Kakenhi (Grant-in-Aid for Scientific Research) in Priority Areas "New strategies for cancer therapy based on advancement of basic research" and the Project on the Materials Development for Innovative Nano-Drug Delivery Systems from the Ministry of Education, Culture, Sports, Science, and Technology of Japan. This work was also supported by the Foundation for Promotion of Cancer Research in Japan.

1. Muggia FM (2001) *Curr Oncol Rep* 3:156–162.
2. Ferrari M (2005) *Nat Rev Cancer* 5:161–171.
3. Hassan M, Little RF, Vogel A, Aleman K, Wyvill K, Yarchoan R, Gandjbakhche AH (2004) *Technol Cancer Res Treat* 3:451–457.
4. Emoto M, Udo T, Obama H, Eguchi F, Hachisuga T, Kawarabayashi T (1998) *Gynecol Oncol* 70:351–357.
5. Duncan R (2006) *Nat Rev Cancer* 6:688–701.
6. Kataoka K, Harada A, Nagasaki Y (2001) *Adv Drug Deliv Rev* 47:113–131.
7. Hamaguchi T, Matsumura Y, Suzuki M, Shimizu K, Goda R, Nakamura I, Nakatomi I, Yokoyama M, Kataoka K, Kakizoe T (2005) *Br J Cancer* 92:1240–1246.
8. Nishiyama N, Okazaki S, Cabral H, Miyamoto M, Kato Y, Sugiyama Y, Nishio K, Matsumura Y, Kataoka K (2003) *Cancer Res* 63:8977–8983.
9. MacKenzie MJ (2004) *Lancet Oncol* 5:541–549.
10. Fuchs CS, Mayer RJ (1995) *N Engl J Med* 333:32–41.
11. Burris HA, III, Moore MJ, Andersen J, Green MR, Rothenberg ML, Modiano MR, Cripps MC, Portenoy RK, Storniolo AM, Tarassoff P, *et al.* (1997) *J Clin Oncol* 15:2403–2413.
12. Watanabe N, Tsuji N, Tsuji Y, Sasaki H, Okamoto T, Akiyama S, Kobayashi D, Sato T, Yamauchi N, Niitsu Y (1996) *Pancreas* 13:395–400.
13. Matsumura Y, Maeda H (1986) *Cancer Res* 46:6387–6392.
14. Maeda H, Matsumura Y (1989) *Crit Rev Ther Drug Carrier Syst* 6:193–210.
15. Sofuni A, Iijima H, Moriyasu F, Nakayama D, Shimizu M, Nakamura K, Itokawa F, Itoi T (2005) *J Gastroenterol* 40:518–525.
16. Takahashi Y, Cleary KR, Mai M, Kitadai Y, Bucana CD, Ellis LM (1996) *Clin Cancer Res* 2:1679–1684.
17. Roberts AB, Wakefield LM (2003) *Proc Natl Acad Sci USA* 100:8621–8623.
18. Feng XH, Derynck R (2005) *Annu Rev Cell Dev Biol* 21:659–693.
19. Bandyopadhyay A, Agyin JK, Wang L, Tang Y, Lei X, Story BM, Cornell JE, Pollock BH, Mundy GR, Sun L-Z (2006) *Cancer Res* 66:6714–6721.
20. Yingling JM, Blanchard KL, Sawyer JS (2004) *Nat Rev Drug Discov* 3:1011–1022.
21. Sawyer JS, Anderson BD, Beight DW, Campbell RM, Jones ML, Herron DK, Lampe JW, McCowan JR, McMillen WT, Mort N, *et al.* (2003) *J Med Chem* 46:3953–3956.
22. Bae Y, Nishiyama N, Fukushima S, Koyama H, Matsumura Y, Kataoka K (2005) *Bioconjug Chem* 16:122–130.
23. Kano MR, Morishita Y, Iwata C, Iwasaka S, Watabe T, Ouchi Y, Miyazono K, Miyazawa K (2005) *J Cell Sci* 118:3759–3768.
24. Dreher MR, Liu W, Michelich CR, Dewhirst MW, Yuan F, Chilkoti A (2006) *J Natl Cancer Inst* 98:335–344.
25. McDonald DM, Choyke PL (2003) *Nat Med* 9:713–725.
26. Gabizon A, Tzemach D, Mak L, Bronstein M, Horowitz AT (2002) *J Drug Target* 10:539–548.
27. Yashiro M, Chung YS, Nishimura S, Inoue T, Sowa M (1996) *Clin Exp Metastasis* 14:43–54.
28. Li DY, Sorensen LK, Brooke BS, Urness LD, Davis EC, Taylor DG, Boak BB, Wendel DP (1999) *Science* 284:1534–1537.
29. Arthur HM, Ure J, Smith AJ, Renforth G, Wilson DI, Torsney E, Charlton R, Parums DV, Jowett T, Marchuk DA, *et al.* (2000) *Dev Biol* 217:42–53.
30. Oh SP, Seki T, Goss KA, Imamura T, Yi Y, Donahoe PK, Li L, Miyazono K, ten Dijke P, Kim S, *et al.* (2000) *Proc Natl Acad Sci USA* 97:2626–2631.
31. Urness LD, Sorensen LK, Li DY (2000) *Nat Genet* 26:328–331.
32. Larsson J, Goumans MJ, Sjostrand LJ, van Rooijen MA, Ward D, Leveen P, Xu X, ten Dijke P, Mummery CL, Karlsson S (2001) *EMBO J* 20:1663–1673.
33. Watabe T, Nishihara A, Mishima K, Yamashita J, Shimizu K, Miyazawa K, Nishikawa S-I, Miyazono K (2003) *J Cell Biol* 163:1303–1311.
34. Hirschi KK, Rohovsky SA, D'Amore PA (1998) *J Cell Biol* 141:805–814.
35. Lebrin F, Deckers M, Bertolino P, ten Dijke P (2005) *Cardiovasc Res* 65:599–608.
36. Fernandez-L A, Sanz-Rodriguez F, Blanco FJ, Bernabeu C, Botella LM (2006) *Clin Med Res* 4:66–78.

Inhibition of Cyclooxygenase-2 Suppresses Lymph Node Metastasis via Reduction of Lymphangiogenesis

Caname Iwata,[1,2] Mitsunobu R. Kano,[1,3] Akiyoshi Komuro,[1] Masako Oka,[1] Kunihiko Kiyono,[1] Erik Johansson,[1] Yasuyuki Morishita,[1] Masakazu Yashiro,[4] Kosei Hirakawa,[4] Michio Kaminishi,[2] and Kohei Miyazono[1,3]

Departments of [1]Molecular Pathology and [2]Gastrointestinal Surgery, Graduate School of Medicine, [3]Center for NanoBio Integration, University of Tokyo, Tokyo, Japan and [4]Department of Surgical Oncology, Medical School, Osaka City University, Osaka, Japan

Abstract

Cyclooxygenase-2 (COX-2) inhibitor has been reported to suppress tumor progression. However, it is unclear whether this inhibitor can also prevent lymphatic metastasis. To determine the effects of COX-2 inhibitor on lymphatic metastasis, etodolac, a COX-2 inhibitor, was given p.o. to mice bearing orthotopic xenografts or with carcinomatous peritonitis induced with a highly metastatic human diffuse-type gastric carcinoma cell line, OCUM-2MLN. Tumor lymphangiogenesis was significantly decreased in etodolac-treated mice compared with control mice. Consistent with this decrease in lymphangiogenesis, the total weight of metastatic lymph nodes was less in etodolac-treated mice than in control mice. Immunohistochemical analysis revealed that the major source of vascular endothelial growth factor-C (VEGF-C) and VEGF-D was F4/80-positive macrophages in our models. The mRNA levels of VEGF-C in mouse macrophage-like RAW264.7 cells, as well as those in tumor tissues, were suppressed by etodolac. The growth of human dermal lymphatic microvascular endothelial cells was also suppressed by etodolac. Supporting these findings, etodolac also inhibited lymphangiogenesis in a model of chronic aseptic peritonitis, suggesting that COX-2 can enhance lymphangiogenesis in the absence of cancer cells. Our findings suggest that COX-2 inhibitor may be useful for prophylaxis of lymph node metastasis by reducing macrophage-mediated tumor lymphangiogenesis. [Cancer Res 2007;67(21):10181–9]

Introduction

Lymph node metastasis is a common occurrence in cancer, and lymphatic vessels serve as an important route for the spread of cancer cells (1, 2). Lymphatic metastasis was previously believed to be a passive process in which detached cancer cells reach lymph nodes through preexisting local lymphatic vessels (3). However, recent studies have suggested that lymphangiogenesis actively contributes to metastasis based on the observations that lymphatic vessel density is correlated with the extent of lymph node metastasis and/or unfavorable prognosis of certain cancers (2, 4, 5). Moreover, some animal tumor models have revealed that expression of lymphangiogenic growth factors leads to formation of lymphatic vessels and that lymphangiogenesis is accompanied by enhanced lymphatic metastasis (2). These findings strongly suggest that lymphatic metastasis can be blocked by inhibition of tumor lymphangiogenesis (1, 6, 7).

The best studied lymphangiogenic signaling system is the vascular endothelial growth factor-C (VEGF-C)/VEGF-D and VEGF receptor 3 (VEGF-R3) signaling axis, which has been shown to play a central role in lymphangiogenesis in animal models (1, 2, 4). Elevated expression of VEGF-C or VEGF-D has been observed in many human cancers (2, 4). A number of studies have shown that levels of expression of VEGF-C in primary tumor correlate with lymphatic vessel invasion and/or lymph node metastasis (2, 4, 8), although the correlation between VEGF-D and metastasis is currently unclear (4, 9). These ligands are thought to be secreted from tumor cells; in addition, macrophages in the peritumoral stroma (i.e., tumor-associated macrophages) have also been reported to produce VEGF-C and VEGF-D in certain cancers and to induce lymphangiogenesis (10). The contribution of inflammatory cells to lymphangiogenesis has also been shown in mouse models of inflammation (11, 12).

Epidemiologic studies have shown that regular intake of nonsteroidal antiinflammatory drugs (NSAID), prototypic inhibitors of cyclooxygenase (COX), such as aspirin, can reduce the risk of development of some cancers (13). In addition, overexpression of COX-2, which is induced by both inflammatory and mitogenic stimuli, is commonly found in many cancers (14–16), suggesting that COX-2 contributes to the process of carcinogenesis. Direct molecular evidence that *COX-2* contributes to carcinogenesis has been obtained from studies in animals engineered to be deficient in expression of the COX-2 gene (17) or treated with COX-2 selective inhibitors (18). Thus far, several mechanisms by which COX-2 contributes to progression of cancer have been reported, including stimulation of proliferation and inhibition of apoptosis of cancer cells, stimulation of cancer cell invasion and angiogenesis, and suppression of immune responses (14, 19).

The major role of COX-2 in angiogenesis is thought to be induction of the synthesis of prostanoids, which then stimulate the secretion of proangiogenic factors, including VEGF-A and fibroblast growth factor-2, from cancer cells and/or stromal fibroblasts (20, 21). In addition, COX-2 stimulates the proliferation (22), migration, and tube formation of vascular endothelial cells (20). Several clinical studies have indeed shown a correlation between level of COX-2 expression and extent of angiogenesis in cancer (23).

In contrast to the effect of COX-2 on angiogenesis, that on lymphangiogenesis remains poorly understood, although correlations between COX-2 expression and lymphangiogenesis or lymph node metastasis have been reported for several human cancers

Note: Supplementary data for this article are available at Cancer Research Online (http://cancerres.aacrjournals.org/).

Requests for reprints: Kohei Miyazono, Department of Molecular Pathology, Graduate School of Medicine, University of Tokyo, 7-3-1 Hongo, Bunkyo-ku, Tokyo 113-0033, Japan. Phone: 81-3-5841-3345; Fax: 81-3-5841-3354; E-mail: miyazono-ind@umin.ac.jp.

doi:10.1158/0008-5472.CAN-07-2366

(24–28). To examine whether COX-2 is involved in lymphatic metastasis, we evaluated the effects of treatment with a COX-2 selective inhibitor, etodolac (29, 30), on tumor lymphangiogenesis and extent of lymph node metastasis using a highly metastatic human diffuse-type gastric carcinoma cell line, OCUM-2MLN (31). We also examined the effects of etodolac on lymphangiogenesis in two other animal models, i.e., a model of carcinomatous peritonitis and one of chronic aseptic peritonitis. Our findings suggest that etodolac has antilymphangiogenic activity *in vivo* and that inhibition of COX-2 could suppress tumor lymphangiogenesis and lymph node metastasis.

Materials and Methods

Animals and cells. Immunodeficient BALB/c nu/nu mice at 4 to 5 weeks of age, obtained from Charles River Laboratories, were used for the model of lymph node metastasis and a model of carcinomatous peritonitis. Specific pathogen-free BALB/c mice at 4 to 5 weeks of age, obtained from Sankyo Laboratory, were used for a model of chronic aseptic peritonitis. Mice were treated in accordance with the policies of the Animal Ethics Committee of the University of Tokyo. OCUM-2MLN, a human diffuse-type gastric carcinoma cell line with a high rate of metastasis to lymph nodes, was previously established (31). RAW264.7, a mouse macrophage-like cell line, was a kind gift from Dr. Tadashi Muroi (NIH Sciences). Human dermal lymphatic microvascular endothelial cells (HDLEC) were obtained from Cambrex.

Model of lymph node metastasis. We used a lentiviral vector (a kind gift from Dr. Hiroyuki Miyoshi, RIKEN; ref. 32) to express the *green fluorescent protein* (*GFP*) gene stably in OCUM-2MLN. A total of 5×10^6 cells in 50 μL of PBS were subserosally inoculated into the gastric walls of BALB/c nu/nu mice as previously described (31) under deep inhalation anesthesia with ether. Four weeks after inoculation, the mice were sacrificed for evaluation. Etodolac (500 ppm in food; obtained from Nippon Shinyaku) or vehicle control was given p.o. throughout the experimental period from the inoculation of cancer cells until evaluation ($n = 7$ mice for each group). The experiment was repeated thrice.

Spread of cancer cells from the site of inoculation in the stomach was observed with a VB-G25 fluorescence stereomicroscope (Keyence). The captured fluorescence images and bright-field images were merged using Adobe Photoshop software (Adobe Systems). All GFP-positive, i.e., metastatic, lymph nodes were collected, and the total weight of these lymph nodes was measured. Stomachs were excised, fixed for 1 h in 10% neutral buffered formalin at room temperature, washed overnight in PBS containing 10% sucrose at 4°C, embedded in optimal cutting temperature compound (Tissue-Tek, Sakura Finetek), and snapped frozen in dry-iced acetone for immunohistochemical examination.

To visualize the lymphatic vessels in normal gastric wall, we injected India ink into the gastric wall of anesthetized control mice and immediately observed the draining lymphatic vessels by stereomicroscope.

Model of carcinomatous peritonitis. We i.p. injected OCUM-2MLN cells (5×10^6) into BALB/c nu/nu mice to induce carcinomatous peritonitis. The mice were sacrificed 2 weeks after inoculation and were evaluated. Etodolac (500 ppm in food) or vehicle control was given p.o. throughout the experimental period from injection of cancer cells until evaluation ($n = 5$ for each group). Diaphragms with disseminated tumor cells were excised, carefully extended, fixed for 30 min in 10% neutral buffered formalin at room temperature, and washed overnight in PBS containing 10% sucrose at 4°C. These diaphragms were embedded in optimal cutting temperature compound and snapped frozen in dry-iced acetone for immunohistochemical study or whole-mount immunostained. The experiment was repeated twice.

To visualize the lymphatic vessels in normal diaphragm, we i.p. injected India ink to control mice and observed the lymphatic vessels filled with ink in the diaphragms 20 min later.

Model of chronic aseptic peritonitis. We i.p. injected 2 mL of 3% thioglycollate medium (BBL thioglycollate medium, BD Biosciences) into BALB/c mice thrice a week for 2 weeks to induce peritonitis. Etodolac (500 ppm in food) or vehicle control was given p.o. during the same period ($n = 5$ for each group). The mice were then sacrificed, and their diaphragms excised and prepared for H&E staining and immunostaining as described above. The experiment was repeated twice.

Immunohistochemistry. Whole mounts of diaphragms and 20-μm cryostat sections of postfixed frozen samples were stained with one or more primary antibodies. We used the following antibodies for immunostaining. For staining of lymphatic vessels, rabbit polyclonal antibody to LYVE-1 (1:200 dilution; Abcam), rat monoclonal antibody to mouse LYVE-1 (1:100 dilution; a kind gift from Drs. Yuichi Oike and Toshio Suda, Keio University), or rabbit polyclonal antibody to Prox1 (1:200 dilution; Chemicon) was used. Rat monoclonal antibody to mouse platelet/endothelial cell adhesion molecule 1 (PECAM-1; 1:200 dilution; BD PharMingen) was used for staining of blood vessels. For staining of VEGF-C and VEGF-D, goat polyclonal antibody to VEGF-C (C-20; 1:50 dilution, Santa Cruz Technology), and rabbit polyclonal antibody to VEGF-D (H-144; 1:50 dilution, Santa Cruz Technology) were used, respectively. Macrophages were immunostained with rat monoclonal antibody to F4/80 (1:20 dilution; Serotec) or rat monoclonal antibody to mouse CD11b (1:200 dilution; Chemicon). Dividing cells were stained with rabbit polyclonal antibody to Ki-67 (1:1,000 dilution; Novo Castra). COX-2 was stained with affinity-purified rabbit polyclonal antibody to COX-2 (1:100 dilution; Cayman Chemical). Subsequently, specimens were incubated with corresponding secondary antibodies labeled with Alexa Fluors 488, 594, or 647 (Invitrogen-Molecular Probes) at 1:200 dilution. Cell nuclei were counterstained with 20 μmol/L TOTO-3 (Invitrogen-Molecular Probes). In control experiments, the primary antibody was omitted. Specimens were examined with a LSM 510 META confocal microscope (Carl Zeiss) or a fluorescence stereomicroscope.

Morphometric analysis. In the model of lymph node metastasis, we double-stained tumor sections for LYVE-1 and PECAM-1 to examine lymphatic and blood vessel densities. For each tumor section, five hotspots (i.e., fields with the highest vascular density) in tumor areas were evaluated at magnification of 200×. Digital images of LYVE-1–positive lymphatic vessels and highly PECAM-1–positive blood vessels were captured. Area densities (percentage of total tissue area) of lymphatic vessels or blood vessels were then calculated using ImageJ software (NIH).

In the model of carcinomatous peritonitis, whole-mount diaphragms stained for LYVE-1 were evaluated from the pleural side. Lymphatic sprouts, defined as tapered projections, were counted at magnification of 100× in 10 microscopic fields per diaphragm.

In the model of chronic aseptic peritonitis, whole-mount diaphragms stained for LYVE-1 and CD11b were evaluated from the peritoneal side. Inflammatory plaques, defined as accumulations of inflammatory cells, especially of macrophages, had formed on the peritoneal surface of the diaphragm. For each diaphragm, 10 microscopic fields in inflammatory plaques were evaluated at magnification of 200×. Digital images of LYVE-1–positive lymphatic vessels were captured, and the area density of lymphatic vessel was calculated using ImageJ software.

RNA isolation and quantitative reverse transcription–PCR. Gastric walls with or without tumor were excised from mice, immersed in RNAlater (Qiagen), embedded in optimal cutting temperature compound, and snapped frozen. Total RNAs were extracted from tissue sections using the RNeasy micro kit (Qiagen). Total RNAs from RAW264.7 and HDLECs were extracted using the RNeasy mini kit (Qiagen). First-strand cDNAs were synthesized using the Quantitect reverse transcription kit (Qiagen) with random hexamer primers. Quantitative real-time reverse transcription–PCR (RT-PCR) analysis was done using the 7500 Fast Real-Time PCR system (Applied Biosystems). The primer sequences used are given in Supplementary Table S1.

Cell growth assay. Cell growth was determined with a WST-8 assay kit (Nacalai Tesque). Briefly, HDLECs (1×10^3 cells per well) or OCUM-2MLN (7.5×10^2 cells per well) in 96-well plates were incubated overnight. Thereafter, the medium was replaced with a new medium containing etodolac and/or lipopolysaccharide (LPS; O111:B4; Sigma-Aldrich). After 24 to 96 h of incubation, the WST-8 reagent was added to the culture. After

2 h of incubation, absorbance at 450 nm was measured with a microplate reader (Bio-Rad).

Statistical analysis. Statistical analysis was carried out using Excel software (Microsoft). Results were compared by Student's *t* test and expressed as mean values with SE. Differences were considered statistically significant at $P < 0.05$. All statistical tests were two-sided. Effects of etodolac on the growth of OCUM-2MLN were evaluated by multivariate ANOVA testing using JMP software (SAS Institute).

Results

Spread of cancer cells via lymphatic vessels in a murine model of lymph node metastasis of gastric cancer. To determine lymph node metastasis *in vivo*, we used an animal model of human metastatic gastric carcinoma, in which OCUM-2MLN cells expressing GFP were inoculated orthotopically into the gastric wall of BALB/c nu/nu mice. Examination by fluorescence stereomicroscope 4 weeks after inoculation revealed that the cancer cells had metastasized from the site of inoculation into the regional lymph nodes. Using this model, we examined tumor lymphangiogenesis and spread of cancer cells through the lymphatic vessels. The cancer cells in this model exhibited invasion into peritumoral lymphatic vessels and spread along lymphatic vessels in the gastric wall toward the regional lymph nodes (Fig. 1*A*). Visualization by intravital injection of India ink into the gastric wall of control mice (Supplementary Fig. S1) revealed that the sizes and numbers of the lymphatic vessels were dramatically increased in the mice inoculated with gastric cancer cells (Fig. 1*A*) compared with those in control mice. To confirm the increase in lymphatic vessels in the mice bearing cancer cells, we double-stained the sections of the gastric wall of the mice using LYVE-1, a specific lymphatic vessel marker, and Ki-67, a marker of cell proliferation. Some dividing lymphatic endothelial cells stained by both LYVE-1 and Ki-67 were observed in the gastric wall of the tumor-bearing mice (Fig. 1*B*), demonstrating induction of lymphangiogenesis in this model.

Suppression of lymphangiogenesis and lymph node metastasis by etodolac in the model of lymph node metastasis. We examined whether etodolac, a COX-2 inhibitor, inhibits

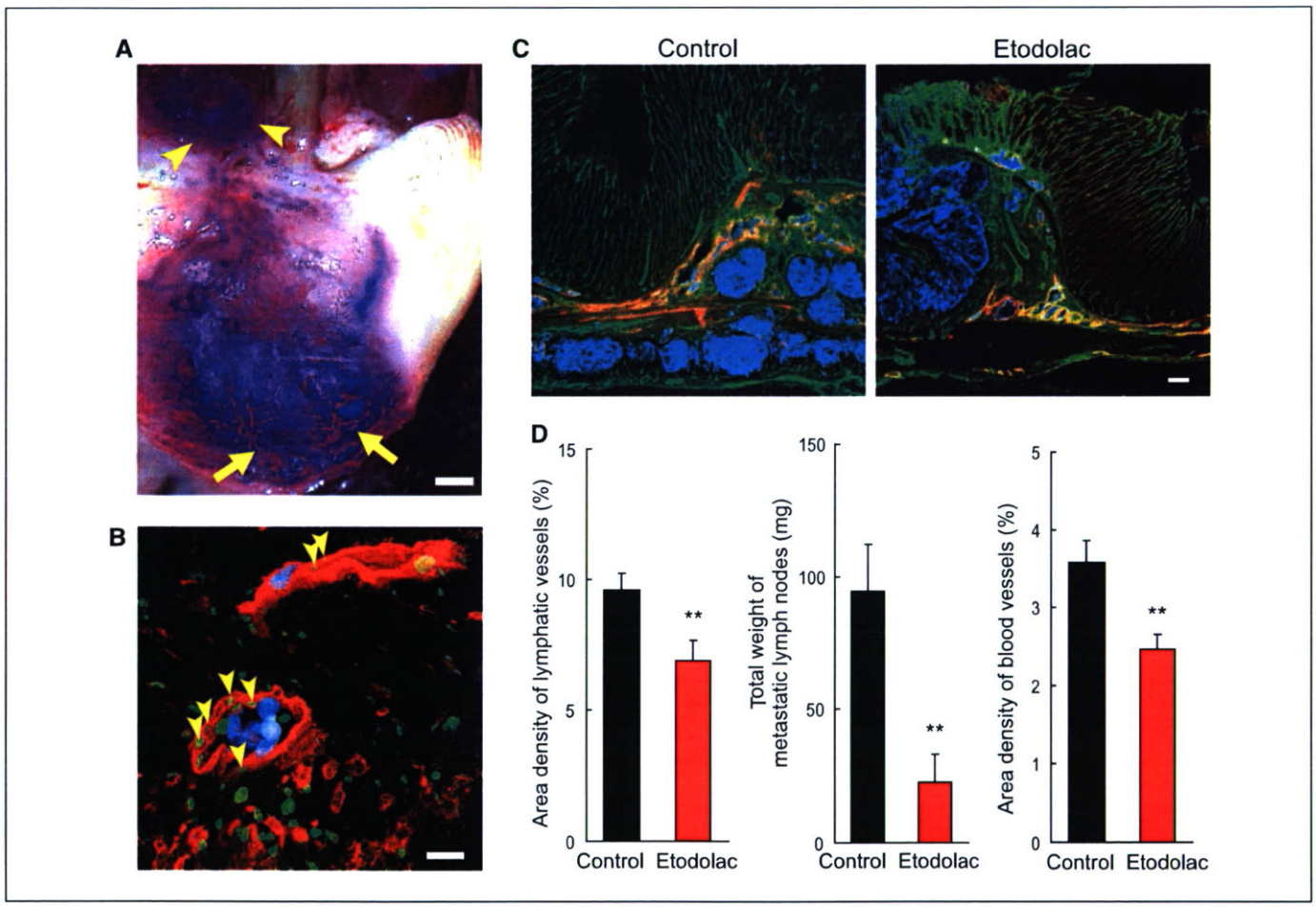

Figure 1. Effects of etodolac on a murine model of lymph node metastasis of gastric carcinoma. *A*, spread of GFP-expressing OCUM-2MLN cells 4 wk after inoculation into gastric wall of BALB/c nu/nu mouse. GFP-positive cancer cells (*purple*) which have invaded peritumoral lymphatic vessels in the gastric wall and metastasized to regional lymph nodes (*arrowheads*). *Arrows*, orthotopically inoculated OCUM-2MLN tumor. *Scale bar*, 1 mm. *B*, cross-section of gastric wall with GFP-positive cancer cells (*blue*), stained for lymphatic vessels (anti–LYVE-1; *red*) and dividing nuclei (anti–Ki-67; *green*). *Arrowheads*, lymphatic endothelial cells positive for Ki-67. *Scale bar*, 20 μm. *C*, orthotopic GFP-positive OCUM-2MLN (*blue*) tumor in control mice or in etodolac-treated mice, stained for lymphatic vessels (anti–LYVE-1; *red*) and blood vessels (anti–PECAM-1; *green*). *Scale bar*, 50 μm. *D, left*, quantification of tumor lymphatic vessels. Columns, mean area density of LYVE-1-positive pixels per microscopic field; *bars*, SE (data from one section per tumor, with 10 images per section). **, $P = 0.008$, two-sided Student's *t* test. *Middle*, total weights of metastatic lymph nodes from control mice and etodolac-treated mice. *Columns*, mean; *bars*, with SE. **, $P = 0.006$. *Right*, quantification of tumor blood vessels. *Columns*, mean area density of pixels highly positive for PECAM-1 per microscopic field; *bars*, SE. **, $P = 0.002$.

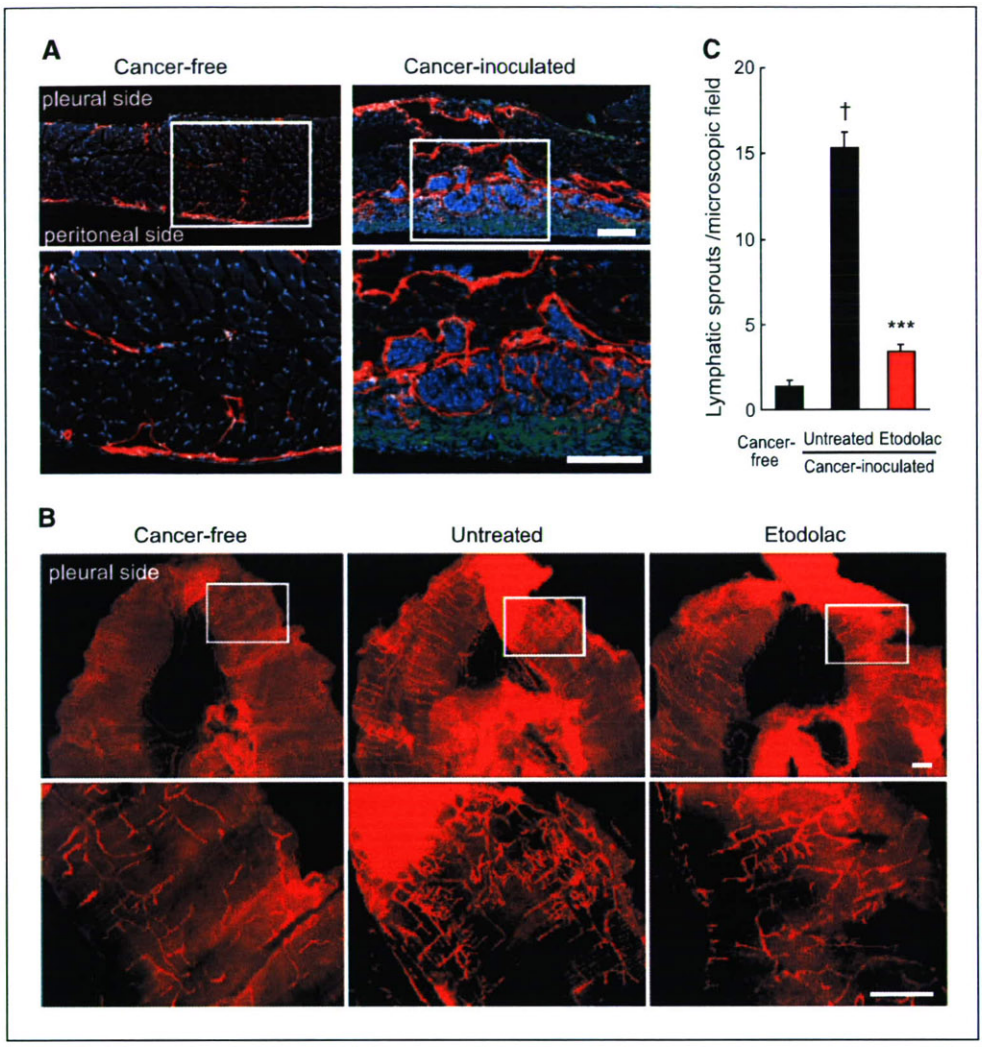

Figure 2. Effects of etodolac on lymphangiogenesis in the model of carcinomatous peritonitis. *A*, lymphatic vessels in the diaphragm in normal mice and those with carcinomatous peritonitis. Immunostaining of lymphatic vessels (anti–LYVE-1, *red*), macrophages (anti-F4/80, *green*), and nuclei (*blue*) in parasagittal sections of the diaphragm from cancer-free mice and those with carcinomatous peritonitis induced by OCUM-2MLN. *Top*, middle magnification; *bottom*, the boxed areas in the top in higher magnification. *Scale bars*, 100 μm. *B*, whole-mount immunostaining for lymphatic vessels (anti–LYVE-1, *red*) of diaphragms from cancer-free mice and those with carcinomatous peritonitis treated with vehicle control or etodolac. *Top*, images of the entire diaphragm at low power; *bottom*, the boxed areas in the top in higher magnifications. *Scale bars*, 1 mm. *C*, quantification of lymphatic sprouts. *Columns*, mean number of lymphatic sprouts per microscopic field; *bars*, SE. $n = 5$ mice for each group and 10 fields per mouse; cancer-inoculated control mice versus cancer-free mice: †, $P < 0.001$; etodolac-treated mice versus cancer-inoculated control mice: ***, $P < 0.001$.

lymphangiogenesis and lymph node metastasis in this model. Etodolac (500 ppm in food) or vehicle control was given p.o. throughout the experimental period, from inoculation of cancer cells to evaluation of lymphangiogenesis and lymph node metastasis. We stained the sections of tumors in the gastric wall for LYVE-1. As shown in Fig. 1*C*, tumor lymphangiogenesis was less prominent in the etodolac-treated mice than in the control mice. Quantification of LYVE-1–positive areas in hotspots confirmed these findings (Fig. 1*D*, *left*). We also determined the extent of lymph node metastasis by measuring the total weight of metastatic lymph nodes identified by expression of GFP using a fluorescence stereomicroscope (Supplementary Fig. S2). Consistent with the decrease in density of lymphatic vessels, the total weight of metastatic lymph nodes was significantly less in etodolac-treated mice than in the control mice (Fig. 1*D*, *middle*).

To determine whether etodolac affects angiogenesis, as well as lymphangiogenesis, we examined tumor angiogenesis by staining sections of tumors for PECAM-1. The relative area occupied by vessels strongly positive for PECAM-1 was significantly decreased in the etodolac-treated mice compared with the control mice (Fig. 1*D*, *right*).

Lymphatic vessels in the diaphragm in normal mice and those with carcinomatous peritonitis. To evaluate tumor lymphangiogenesis in another fashion, we established a new model of lymphangiogenesis, in which the lymphatic vessels of the diaphragm of mice can be observed. We first observed the physiologic function and morphologic characteristics of lymphatic vessels in the diaphragm. Only 20 min after the injection of India ink into the abdominal cavity, lymphatic vessels in the diaphragm were stained with the ink (Supplementary Fig. S3*A*). Lymphatic vessels in the diaphragm were also observed by whole-mount immunostaining for LYVE-1 and Prox1 as specific markers of lymphatic vessels (Supplementary Fig. S3*B*). Immunostaining of sections of the diaphragm for LYVE-1 revealed a lymphatic network consisting of lymphatic lacunae on the peritoneal side and intermuscular lymphatic vessels (Fig. 2*A*, *left*; ref. 33).

Next, we observed the diaphragms of mice with carcinomatous peritonitis. Two weeks after i.p. inoculation of OCUM-2MLN cells (5×10^6) into BALB/c nu/nu mice, cancerous ascites had accumulated, and dissemination of cancer on the peritoneal surface of the diaphragm was observed (data not shown). Sections of diaphragm revealed that these sites of dissemination consisted of cancer cells and F4/80-positive macrophages (Fig. 2*A*, *right*). The lymphatic vessels in the diaphragm were increased in both size and number. Outgrowths of the lymphatic vessels into the site of dissemination were also detected (Fig. 2*A*).

Suppression of lymphangiogenesis by etodolac in the model of carcinomatous peritonitis. As described above, lymphatic